



Quantifying the long-range structure of foams and other cellular patterns with hyperuniformity disorder length spectroscopy

A. T. Chieco  and D. J. Durian *Department of Physics and Astronomy, University of Pennsylvania, Philadelphia, Pennsylvania 19104-6396, USA*

(Received 18 December 2020; accepted 21 May 2021; published 10 June 2021)

We investigate the local and long-range structure of several space-filling cellular patterns: bubbles in a quasi-two-dimensional foam, and Voronoi constructions made around points that are uncorrelated (Poisson patterns), low discrepancy (Halton patterns), and displaced from a lattice by Gaussian noise (Einstein patterns). We study local structure with distributions of quantities including cell areas and side numbers. The former is the widest for the bubbles making foams the most locally disordered, while the latter show no major differences between the cellular patterns. To study long-range structure, we begin by representing the cellular systems as patterns of points, both unweighted and weighted by cell area. For this, foams are represented by their bubble centroids and the Voronoi constructions are represented by the centroids as well as the points from which they are created. Long-range structure is then quantified in two ways: by the spectral density, and by a real-space analog where the variance of density fluctuations for a set of measuring windows of diameter D is made more intuitive by conversion to the distance $h(D)$ from the window boundary where these fluctuations effectively occur. The unweighted bubble centroids have $h(D)$ that collapses for the different ages of the foam with random Poissonian fluctuations at long distances. The area-weighted bubble centroids and area-weighted Voronoi points all have constant $h(D) = h_e$ for large D ; the bubble centroids have the smallest value $h_e = 0.084\sqrt{\langle a \rangle}$, meaning they are the most uniform. Area-weighted Voronoi centroids exhibit collapse of $h(D)$ to the same constant $h_e = 0.084\sqrt{\langle a \rangle}$ as for the bubble centroids. A similar analysis is performed on the edges of the cells and the spectra of $h(D)$ for the foam edges show $h(D) \sim D^{1-\epsilon}$ where $\epsilon = 0.30 \pm 0.15$.

DOI: [10.1103/PhysRevE.103.062609](https://doi.org/10.1103/PhysRevE.103.062609)

I. INTRODUCTION

There are many known ways to quantify the local structure of foams and other cellular systems using cell size, shape, topology, and neighbor correlations [1–4]. Distributions of such local measures are used to describe the entire foam packing, and under proper normalization they remain the same as the foam coarsens; i.e., they exhibit statistical self-similarity [5–13]. By contrast, quantifying the long-range structure of foams and other cellular systems remains an open question.

Recently the concept of hyperuniformity was introduced regarding the structure in disordered materials at long distances [14–16]. Materials are called hyperuniform if long-range density fluctuations are suppressed to the same extent as in crystals. Work on hard-particle packings of bidisperse disks, ellipses, and superballs at the jamming transition found they are hyperuniform, leading to the hypothesis that hyperuniformity exists in all systems at the jamming transition regardless of particle shape or polydispersity [17–19]. Analysis of a wide assortment of other disordered materials at or slightly below the jamming transition finds signatures of hyperuniformity [20–25]. However, hyperuniformity is not a signature of all jammed systems: Work on simulated packing of bidisperse soft disks shows it does not exist above the jamming transition [26–28]. Additionally, Ref. [28] shows for two dimensions and Ref. [27] shows for three dimensions that systems above jamming are both not hyperuniform and their

overall uniformity decreases as the distance above jamming increases. This is where foams pose an interesting problem. Ideally dry foam is far above the jamming transition and hence should not be hyperuniform, yet it is completely space filling and the total absence of density fluctuations makes it trivially hyperuniform. Nevertheless the bubble packing structure and the distribution of liquid films are visually disordered, possessing large spatial density fluctuations that could impact behavior and need to be quantified.

While foams are a naturally occurring cellular packing, this same problem exists for any disordered system with global packing fraction $\phi = 1$. To examine this problem in detail we generate space-filling cellular packings by partitioning space with Voronoi constructions around point patterns of varying disorder. Such packings were analyzed in recent studies with regards to their long-range uniformity and other properties [29–31]. In Ref. [30] the authors, using a standard method for diagnosing hyperuniformity, find that the small- q wave vector scaling of the spectral density behaves like $\chi(q) \sim q^4$ where the exponent is exact based on the conditions of their simulation. They do not present experimental data, so we perform the same kind of Fourier analysis as they do but on our foam systems as well as on our simulated Voronoi constructions. Since all of the packings closely mirror the conditions analyzed in Ref. [30], we are interested in whether analyzing our systems recover the same spectral density scaling exponent. This also allows us to test the extent to which foams are hyperuniform.

More generally we compare the uniformity of their long-range structure to the other space-filling cellular patterns, using both Fourier space and real space methods.

In real space, testing for hyperuniformity is done by randomly placing a series of local observation windows throughout a sample, measuring the area fraction covered by the particles that land within each window and calculating the variance of the measured set of area fractions. This is repeated for growing observation windows, and if at large length scales the variance is suppressed to the same extent as in crystals then the system is said to be hyperuniform. There are two ways to define the area fraction within a measuring window. One method calculates the area covered by a particular phase of the media that lands inside the window. If a cellular packing has global packing fraction $\phi = 1$ then every measuring window finds a local area fraction $\phi_w = 1$ and no meaningful signature of hyperuniformity can be found. The other method, which we employ here, defines a cell as a point weighted by the area of the cell; any points that land inside the local observation window have the entire area of their cell counted, but points that land outside the observation window have none of their area counted.

Measuring the asymptotic scaling behavior at small q or at large lengths provides an answer to whether these systems are hyperuniform but does not provide additional insight into the actual structure of the underlying pattern. This can be done in principle using the same tools for diagnosing hyperuniformity in real space but a necessary step is converting the fluctuations observed in a local measurement window into a length scale; this length scale is called the hyperuniformity disorder length h and its size is the average distance from the boundary of a local measurement window where the particle number density fluctuates [32,33]. Therefore the value of h provides us with an intuitive length scale for disorder that probes the nature of long-range structure as well as the structure at smaller distances. This technique is called “hyperuniformity disorder length spectroscopy” (HUDLS) and has shown success in identifying long-range structure for other soft systems [28]. Here we use it to uncover and compare the extent of potential hidden order of various structural features of foam and other cellular patterns. We are also able to determine whether the local structure informs long-range structure.

II. METHODS

A. Hyperuniformity: Scaling and definitions

In this section we begin with a review of established methods used to diagnose hyperuniformity in ways that quantify long-range structure; expert readers may skip to Sec. II B. Hyperuniformity is diagnosed by measuring the asymptotic scaling of either the spectral density $\chi(q)$ for small q or the variance $\sigma_\phi^2(D)$ in the set of local volume fractions measured in randomly placed windows of diameter D for large D . A scaling exponent ϵ relates the two quantities. If the spectral density has small wave vector behavior like $\chi(q) \sim q^\epsilon$ with $\epsilon > 0$, or more generally if $\chi(0^+) = 0$, then a system is said to be hyperuniform; small- q scaling with $0 < \epsilon \leq 1$ corresponds to the long length scaling $\sigma_\phi^2(D) \sim 1/D^{d+\epsilon}$ where d is dimensionality; for $\epsilon \geq 1$, $\chi(q) \sim q^\epsilon$ corresponds to

$\sigma_\phi^2(D) \sim 1/D^{d+1}$ and we say the system is strongly hyperuniform. By contrast, ordinary systems exhibit Poissonian fluctuations where $\epsilon = 0$. In reciprocal space the spectral density is $\chi(0^+) = C$ where $C > 0$ is some constant and in real space the volume fraction variance scales like $\sigma_\phi^2(D) \sim 1/D^d$ according to the dimensionality. While the exponent ϵ can be used as a proxy for order, its actual value does not have a direct physical interpretation. Instead of the exponent ϵ , we derive meaning from the actual values of the $\chi(q)$ and $\sigma_\phi^2(D)$ by use of different means in reciprocal and real space as follows.

For the spectral density, some intuition is achieved by choosing a proper normalization of $\chi(q)$ according to the spectral density for a Poisson pattern where particles are placed totally at random. If a cellular patterns in two dimensions is represented by a central-point with the entire area a_j of particle j is at the location \mathbf{r}_j of its center then a suitably normalized definition of the spectral density is

$$\chi(q) \equiv \left(\sum a_j e^{i\mathbf{q}\cdot\mathbf{r}_j} \sum a_k e^{-i\mathbf{q}\cdot\mathbf{r}_k} \right) / \sum a_j^2, \quad (1)$$

where $q = |\mathbf{q}|$ for isotropic packings and the sums are over all particles. This normalization means Poisson patterns have $\chi(q) = 1$, which becomes a nominal upper bound and insight into structure at a given q is extracted from how far $\chi(q)$ lies below this value. Another benefit of this normalization is for systems of monodisperse particles or for point patterns the spectral density reduces to the structure factor, $S(q)$.

In real space, structure is quantified intuitively by the spectrum of hyperuniformity disorder lengths $h(D)$; full details and examples may be found in Refs. [28,32,33], and are given more briefly in the remainder of this section. Determining $h(D)$ for two-dimensional systems begins by finding the variance $\sigma_\phi^2(D)$ for a set of local area fractions $\sum N_i a_i / A_\Omega$, where N_i is the number of particles of species i whose centers lie inside a randomly placed window of area $A_\Omega = \pi(D/2)^2$ and the sum is over species. This is the real space definition of the central point representation. Using these definitions a completely random arrangement of particles will have $\sigma_\phi^2(D) = \langle a \rangle / A_\Omega$ where $\langle a \rangle = \sum \phi_i a_i / \sum \phi_i$ is the area fraction weighted average particle area, ϕ_i is the area fraction covered by particles with a_i , and $\phi = \sum \phi_i$ is the area fraction of all the particles in the system.

The measured area fractions fluctuate depending on where the measuring window is within the system due to differences in the number and sizes of particles landing inside the window; hyperuniform configurations have fluctuations that are understood to be due to particles at the surface of the measuring windows [14]. However, particle centers do not actually lie *on* the window surface. Instead, it is more appropriate to picture fluctuations as determined by the average number of particles whose centers lie inside the window within some distance h of the surface; this is shown pictorially for a circular window in Fig. 1. For circular windows with area $A_\Omega = \pi(D/2)^2$, we can thus define h from the number variance via $\sigma_{N_i}^2 \equiv (\phi_i/a_i)\pi[(D/2)^2 - (D/2 - h)^2]$, where the right-hand side is simply the average number of particles of species i whose centers lie in the green annulus. The number variance is then converted to an area fraction variance using $\sigma_\phi^2 = \sum \sigma_{N_i}^2 a_i^2 / A_\Omega^2$. Finally, averaging over species leads to the

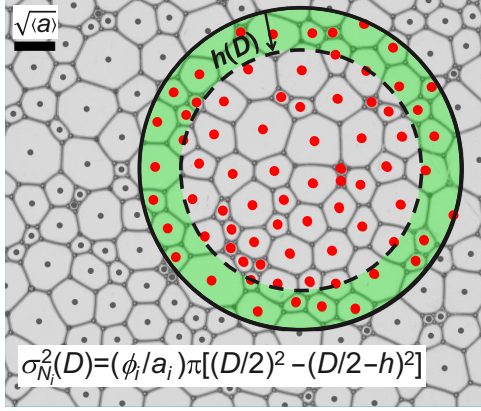


FIG. 1. Image of a quasi-two-dimensional (quasi-2D) foam with the bubble centroids marked by dots. The total area of bubbles enclosed in a circular window is taken as the sum of areas for bubbles whose centroids land within the window (large filled circles). The area fraction variance is controlled by the number of particles in the shaded region of thickness $h(D)$, averaged over window placements. As depicted here for $D = 8\sqrt{\langle a \rangle}$, the hyperuniformity disorder length is $h(D) = \sqrt{\langle a \rangle}$ where $\langle a \rangle$ is the area-fraction weighted average bubble area. The value of $h(D)$ is inflated by over $10\times$ its actual value for illustrative purposes.

following explicit definition of $h(D)$ in terms of the measured variance:

$$\frac{\sigma_\phi^2(D)}{\phi} \equiv \frac{\langle a \rangle}{\pi(D/2)^2} \left\{ 1 - \left[1 - \frac{h(D)}{D/2} \right]^2 \right\}, \quad (2)$$

$$\approx 2 \frac{\langle a \rangle h(D)}{(D/2)^3} \text{ for } D \gg h(D). \quad (3)$$

These expressions were given in footnote 2 of Ref. [28]. Note that smaller $h(D)$ means smaller fluctuations and more uniformity, while larger $h(D)$ means more disorder. Furthermore, $\sigma_\phi^2(D) \sim 1/D^{d+\epsilon}$ corresponds to $h(D) \sim D^{1-\epsilon}$; therefore, Poissonian fluctuations have $\epsilon = 0$ and correspond to $h(D) \sim D$, and the upper bound is $h(D) = D/2$ for a Poisson pattern where all particles inside the measuring window contribute to area fraction fluctuations. Strong hyperuniformity where $\epsilon \geq 1$ corresponds to a large- D asymptote that is constant: $h(D) = h_e$ and particles inside the window further than h_e do not contribute to measured fluctuations. For this case, $\sigma_\phi^2(D) \sim \langle a \rangle h_e / D^3$ is made dimensionally correct by the existence of h_e as an emergent length rooted in the intuitive notion of what it means to be hyperuniform. Thus h_e is the desired measure of structure that is independent of D when the system is hyperuniform, and Eq. (2) generalizes upon this to systems with any degree of uniformity.

The definitions for the hyperuniformity disorder length are discussed in much more detail in Refs. [28,32,33]. These references also go through the calculations of the upper bound $h(D) = D/2$ as well as a lower bound for the separated-particle limit where the size of the measuring window is smaller than the average distance between two particles.

We also note that hyperuniformity is truly a measure of number fluctuations and because points are given a weight

equal to their area the above discussion is in the context of long wavelength area fraction fluctuations. However, using the central point representation fluctuations in any order parameter can be determined by assigning an appropriate weight to each point, i.e., for fluctuations in coordination number each point is given a weight equal to its number of contacts [34]. Assigning equal weight to each point makes the system monodisperse and it is treated simply as a point pattern; the signature of hyperuniformity for these systems is fluctuations in the number variance that grow more slowly than the volume of the window. This treatment changes the definitions and bounds from above: the spectral density reduces to the structure factor $S(q)$ and all particle areas are $a_j = 1$; the random expectation for the number variance is $\sigma_N^2(D) = \rho A_\Omega$ where ρ is the number density. The definition of $h(D)$ also changes and is defined by rearranging $\sigma_N^2 = \rho\pi[(D/2)^2 - (D/2 - h)^2]$; $h(D)$ whether defined from the number variance or the area fraction variance is calculated from a ratio of the measured variance to the expected variance for a totally random system in both cases and our intuition for what it measures remains the same. Because foams have not been studied in the context of hyperuniformity, we explore our systems both as monodisperse point patterns using the centroids of the bubbles and as polydisperse systems where the centroids are weighted by their bubble area.

B. Foam and Voronoi data

We study foam made from a solution that is 75% deionized water, 20% glycerin, and 5% Dawn Ultra Concentrated Dish Detergent. It is generated inside a sample cell made from two 1.91 cm-thick acrylic plates separated by a spacing of 0.3 cm and sealed with two concentric o rings, the inner of which has a 23 cm diameter; this is the same apparatus used in Ref. [35] for foam coarsening experiments. Foams are produced as follows. First the trough is filled with the desired amount of liquid, then flushed with nitrogen and sealed. The entire sample cell is vigorously shaken for several minutes until the gas is uniformly dispersed as bubbles that are smaller than the gap between the plates. The foam is thus initially very wet, opaque, and three dimensional. The cell is immediately placed above a Vista Point A light box and below a Nikon D90 camera with a Nikkor AF-S 300mm 1:2.8D lens. After a few hours, the bubbles become large compared to the gap and the foam has coarsened into a quasi-two-dimensional state; thereafter, images are acquired every 2 min for 24 h.

To extract relevant data for bubbles, such as their locations and areas, we first have to reconstruct the foam microstructure and film network. The reconstruction methods are described more thoroughly in the Supplemental Materials of Ref. [36]. Briefly, the first step is to locate the vertices via a convolution method using an example vertex structuring element and the foam image. After the vertex locations are identified they are connected to their neighbors by exploiting Plateau's law that the vertices are the junction of three films meeting at 120° and that pairs of vertices are connected by films that are circular arcs. Finally bubbles are identified by making closed loops of vertices.

To perform the above hyperuniformity analyses, the foams need to be represented by points. The bubble centroids are a

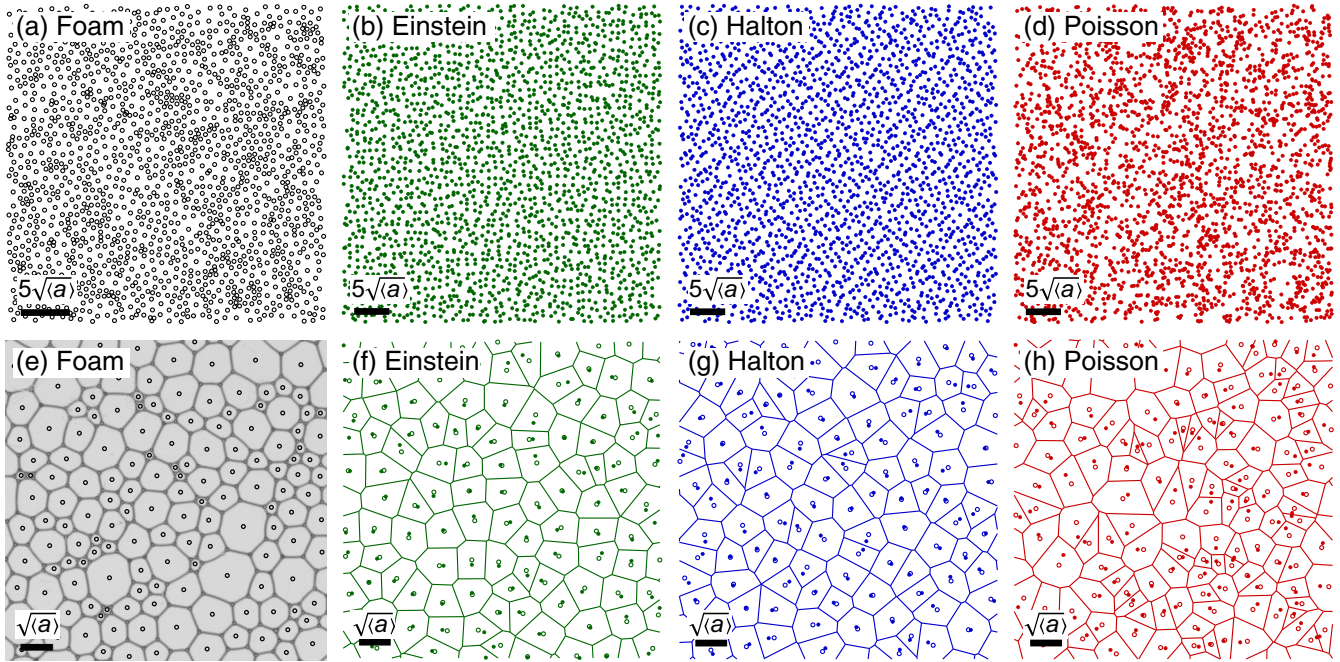


FIG. 2. Disordered points patterns: (a) the locations of the centroids of the bubbles in a quasi-two-dimensional foam; (b) an Einstein pattern where points are randomly displaced from a square lattice with root mean square displacement $\delta/b = 0.26$ where b is the lattice spacing; (c) a Halton set, which is a low discrepancy pattern where points are determined algorithmically; (d) a Poisson pattern where points are placed totally at random. (e)–(h) show the cellular patterns that partition space around the point patterns as labeled: (e) displays the bubbles of a quasi-2D foam as well as the bubble centroids; (f)–(h) show the cells of a Voronoi construction, which are created around the filled circles that occupy each cell. In all parts open circles are used for particle centroid patterns and filled circles show points used to generate Voronoi constructions. For analysis of area fraction fluctuations all points are given a value equal to the area of the cell they occupy.

logical choice, as given by

$$x_c = \sum (x_i + x_{i+1})(x_i y_{i+1} + x_{i+1} y_i) / (6\alpha), \quad (4)$$

$$y_c = \sum (y_i + y_{i+1})(x_i y_{i+1} + x_{i+1} y_i) / (6\alpha), \quad (5)$$

$$\alpha = \sum (x_i y_{i+1} + x_{i+1} y_i) / 2, \quad (6)$$

where the sums are between all neighboring pairs of vertices on a bubble. An example of the large-scale point pattern and a zoomed-in version are shown in Figs. 2(a) and 2(e), respectively.

To understand the nature of the disorder in the location of bubble centroids, we compare three different types of pattern. The first is an Einstein pattern; these consist of points initially placed on a square lattice and then randomly displaced by kick sizes drawn from a Gaussian distribution. Varying the root mean square (RMS) displacements of the particles will tune the disorder in the patterns [32]. Here we set the standard deviation to be $\delta = 0.26b$, where b is the lattice spacing. This gives the same number variance as for the second type of pattern, known as Halton patterns. These use points from a low discrepancy sequence [37]. They are of general interest because although they are noncrystalline they fill space quite evenly, making them and other low discrepancy patterns useful in, e.g., Monte Carlo integration [38–40]. Creating a Halton pattern in two dimensions is done by choosing two integers $\{j_1, j_2\}$ whose only common denominator is 1; each number is an independent seeding element for a list of

numbers. For our patterns we take $j_1 = 2$ and $j_2 = 3$. The n th number in the sequence is determined by converting n into a number with base j_k , writing the number in reverse order after a decimal point and converting this fraction back into base 10 representation. This is done for both seeding elements and the pair of numbers creates one point in the Halton pattern. The final cellular pattern is a Poisson pattern where uncorrelated points are laid down by drawing numbers from a high-quality random number generator. Figures 2(b)–2(d) shows the sample point patterns.

Bubbles, however, are not simply points but are actually highly polydisperse cells of a larger space-filling pattern. Therefore we also study how the areas of bubbles are distributed throughout space. For this analysis to keep with the definitions for $\chi(q)$ and $h(D)$ from Eqs. (1) and (2), the bubble centroids are given a weight equal to the area of the bubble they occupy. To find the areas, the bubbles are first treated as polygons and the polygonal areas are calculated using Eq. (6). The curved edges of the bubbles are not accounted for in this initial calculation. Accounting for this additional area, the final calculation of the area of any bubble is its polygonal area plus or minus the area under each of the circular arcs if the arc bends away or towards from the centroid of the bubble, respectively. The foams are space filling and have a packing fraction of $\phi = 1$.

Similar to the point pattern analysis, we want to compare data from bubbles to data from other cellular structures. In simulation we are free to partition space, however, we choose as long as we maintain a packing fraction $\phi = 1$; for this study

we create cellular patterns from Voronoi constructions around the three types of simulated point patterns described earlier in this section. A Voronoi construction tiles space by separating points into cells whose edges are lines equidistant from the two points that share that edge. Voronoi patterns are generated using an intrinsic MATLAB function and this function also identifies the locations of the vertices for each cell. All cells are polygons meaning only Eq. (6) is needed to calculate the cell area. Voronoi constructions, especially those made around Poisson patterns, have been studied extensively but much of the work is beyond the scope of this paper [41]; here they are used to study the structure of cellular patterns that are built around point patterns of known disorder and compare that to the structure of quasi-2D foams, which are cellular patterns that surround point patterns of unknown disorder. Recently work on cellular patterns in the context of hyperuniformity by partitioning space using several methods including Voronoi constructions was published [30,31]; it does not include any experimental data nor does it consider the hyperuniformity disorder length.

III. RESULTS

Using the methods described above we reconstruct three snapshots of the same foam as it coarsens. They are taken $\{6, 10, 18\}$ h after its initial preparation and have $N = \{2767, 1842, 1099\}$ bubbles, respectively. The total number N of bubbles decreases with time as the foam coarsens, whereby smaller bubbles shrink away and larger bubbles grow due to differences in Laplace pressure. This is accompanied by an increase in both the mean bubble area $\bar{a} = \sum a_i/N$ and the ϕ -weighted average bubble area $\langle a \rangle = \sum a_i^2 / \sum a_i$. Individual foam data sets are referred to by the latter: $\langle a \rangle = \{10, 15, 25\}$ mm². For the simulated patterns, the Voronoi constructions are made in a square box bounded by $(0, 1)$ with $N \geq 4.97 \times 10^5$ cells each. This is large enough that only one pattern of each type is generated and analyzed.

A. Bubble-scale quantities

Though it is not our main interest, for orientation and completeness we start by investigating several standard local structural features, beginning with the distribution of bubble areas. Figure 3(a) shows the cumulative distribution function for the bubble areas normalized by the mean bubble area for the three snapshots of the coarsening foam. Evidently, the data collapse nicely, as expected for a foam that has coarsened into the self-similar scaling state. Statistically, older foams appear the same as taking a smaller subsection of a younger foam with the same number of bubbles. Self-similarity is well documented and has been observed in experiment [5–8] and simulation [9–13]. It is once again found here, where the data fit well to a slightly compressed exponential consistent with previous work [2,3,35].

In addition to providing insight into the local structure of the foam the collapse of these distributions serves two more purposes. First it shows our methods for calculating the bubble areas are correct, which is very important for our hyperuniformity analysis. Second because the foam is self-similar the data from the three images can be collected together to make

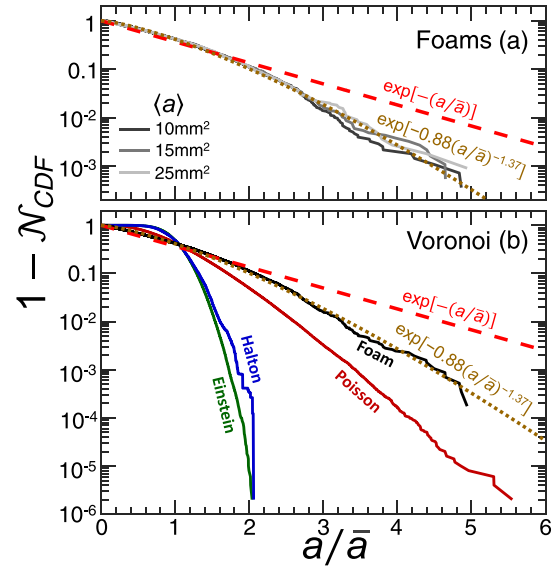


FIG. 3. Cumulative distribution function data for (a) bubble areas for foam as it coarsens and (b) areas of Voronoi cells constructed around point patterns as labeled. In (a) the bubble areas collapse after normalizing by the mean area \bar{a} . In (b) all the foam data are collected into one distribution and plotted as the black curve. In both parts the red dashed line shows an exponential area distribution and the gold dotted curve is a compressed exponential.

one distribution with better statistics. This is done for the normalized bubble areas and the data are plotted in Fig. 3(b) as a black curve. Comparing the cumulative distributions of cell areas for the Voronoi constructions to those of the bubble areas for the foam show the latter is the widest. In this sense, the local structure of the foam is the most disordered. The distributions of cell areas for the Voronoi constructions show that cells generated around the Einstein and Halton patterns have the most local order, with nearly identical distributions. The cells generated around the Poisson patterns have a local order between Einstein or Halton and the foams. One way to quantify the local disorder is thus by the width of the area distributions, or equivalently by the dimensionless ratio \bar{a}^2/\bar{a}^2 . The values extracted from the data are collected in Table I. These increase with increasing disorder, and are less than the value $\bar{a}^2/\bar{a}^2 = 2$ for an exponential distribution.

In addition to \bar{a}^2/\bar{a}^2 , another good measure of bubble-scale structure is the dimensionless shape parameter $E = P/\sqrt{4\pi A}$, known as elongation, computed for each bubble by the ratio of its perimeter to square root of area and scaled to be $E = 1$ for circular bubbles. Reference [35] finds elongation to be one of two dimensionless shape parameters important in the dynamics of foam coarsening with the other being circularity. Calculating the elongation for all bubbles and collecting them into one distribution, we compare the data to the elongation of the Voronoi cells. The cumulative distributions are shown in Fig. 4 and the inset of the figure is a zoom in for the small E data. The distribution for the foam is not the widest as it was for the areas but instead is smaller than the Poisson and goes farther than both Halton and Einstein. We show the average elongation and the average squared elongations in Table I and in both cases these values are ordered from low to high as

TABLE I. Local quantities characterizing cell size and shape in the four types of space-filling cellular patterns: average squared area divided by the average area squared, the average number of sides of a cell, the standard deviation for the side-number distribution, the average elongation, the average squared elongation, and the average squared edge length divided by the average edge length squared. Data for all bubbles at the three times are collected into one distribution because the foam is in a self-similar state.

Pattern	$\overline{a^2}/\overline{a}^2$	\bar{n}	σ_n	\bar{E}	$\overline{E^2}$	$\overline{s^2}/\bar{s}^2$
Einstein	1.05 ± 0.002	5.99 ± 0.01	0.993 ± 0.002	1.127 ± 0.0001	1.271 ± 0.002	1.29 ± 0.03
Halton	1.06 ± 0.002	5.99 ± 0.01	1.092 ± 0.002	1.142 ± 0.0001	1.308 ± 0.002	1.33 ± 0.04
Poisson	1.28 ± 0.006	5.99 ± 0.01	1.332 ± 0.002	1.181 ± 0.0002	1.403 ± 0.003	1.42 ± 0.04
Foam	1.82 ± 0.07	5.98 ± 0.08	1.17 ± 0.02	1.10 ± 0.02	1.22 ± 0.03	1.19 ± 0.01

foam, Einstein, Halton, and Poisson. Foam has the smallest average values because the data plunge away from 1 the fastest which is seen clearly in the inset of Fig. 4.

The four types of cellular pattern are further compared and contrasted in Fig. 5 by examining the contribution to the full elongation distribution by cells with different side numbers, n . Figure 5(a) shows the data for the foam where data with small E have large n and bubbles with a smaller number of sides have larger E values. Interestingly the foam have regions with little to no overlap for different n -sided bubbles; this is exhibited by the peaks of the individual n -sided distributions nearly matching the entire distribution especially for bubbles with less than seven sides. For the Voronoi packings these regions of little overlap do not exist and the peaks of the distributions are not separated. Only the foams have well-separated elongation distribution for different n -sided cells.

Other standard distributions we study include the side-number distribution $p(n)$, which tells the probability of finding a bubble or cell with n sides and the area-weighted side-number distribution $F(n)$, which tells the fraction of sample area that is covered by n -sided bubbles or cells. The distributions for $p(n)$ and $F(n)$ are plotted in Figs. 6(a) and 6(b), respectively. The $p(n)$ distributions are remarkably similar, which is expected given that both the bubbles and Voronoi cells are convex polyhedra where the vertices are a junction of three edges; this microstructure also makes it so the average number of sides per cell is $\bar{n} = 6$ and Table I shows this is

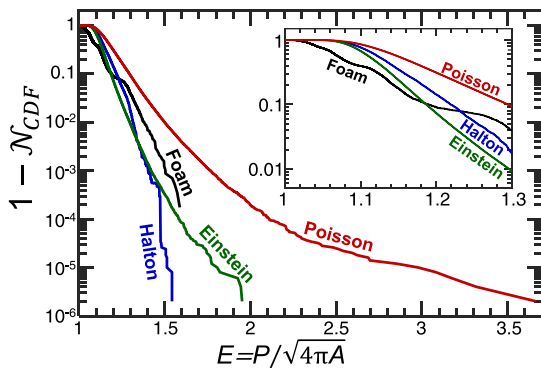


FIG. 4. Cumulative distribution of the elongation shape parameter for the various cellular patterns, as labeled. The foam data is collected from the combined data from the three different times during the aging process. The distributions have statistical uncertainties described in Ref. [35], with error bars that are smaller than the symbols.

almost exactly achieved for all packings. Figure 6(b) shows the $F(n)$ distribution for the foam is skewed more towards cells with large n when compared to the other distributions particularly for bubbles with $n = \{7, 8\}$ sides. This is understood because bubbles with a larger number of sides also have larger areas. These distributions allow us to understand the local structure of the cellular patterns but next we investigate whether they provide any insight into the long-range structure.

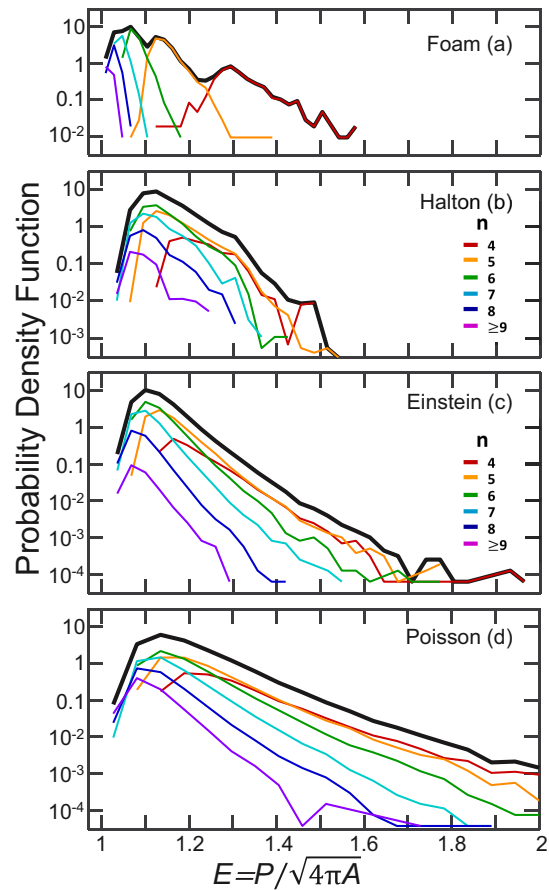


FIG. 5. Distribution of the elongation shape parameter for different cellular patterns, as labeled. The full distribution is plotted as a thick curve, and data for n -sided cells are colored according to the number of sides. The foam data is collected from the combined data from the three different times during the aging process.

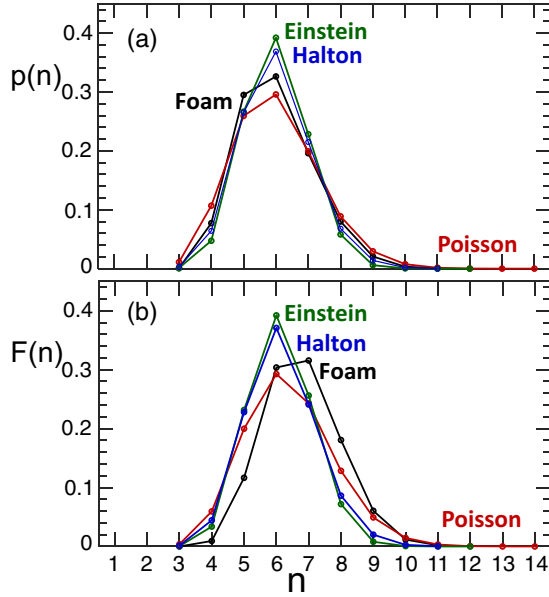


FIG. 6. (a) Side-number distributions, and (b) area-weighted side-number distributions, for the various cellular patterns, as labeled. The foam data is collected from the combined data from the three different times during the aging process. The distributions have statistical uncertainties described in Ref. [35], with error bars that are smaller than the symbol sizes.

B. Spatial density fluctuations

We now present our main results quantifying spatial variation in each of the four types of cellular patterns. Specifically, hyperuniformity and the nature of density fluctuations at both short and long length scales are diagnosed by the spectral density, $\chi(q)$, and by the real space spectra of hyperuniformity disorder lengths, $h(D)$, respectively, computed from Eqs. (1)–(2). Throughout, length scales are normalized by the square root of the ϕ -weighted average cell area $\sqrt{\langle a \rangle}$. We begin with number density fluctuations, where cells are considered as points of equal weight (i.e., equal area) such that $\chi(q)$ reduces to the structure factor $S(q)$. Then we turn to fluctuations of area fractions, followed by cell boundaries. Finally, we compare various spectra for the foam samples.

1. Hyperuniformity of number density

We first treat the cellular structures as patterns of points, using both the centroids of the bubbles and Voronoi cells as well as the points around which the latter were constructed. By eye, the images in Figs. 2(a)–2(d) show that foam and Poisson point patterns exhibit more low-density voids and also more high-density clumps than the Einstein and Halton point patterns, where the points are more uniformly distributed. Figure 2(e)–2(h) show that the centroids are slightly shifted to make the patterns more uniform but only at the cellular scale. This is reflected in both the small- q scaling of $S(q)$ data, and in the large- D scaling of $h(D)$ data, displayed in Fig. 7, for both points [Figs. 7(a)–7(b)] and centroids [Figs. 7(c)–7(d)]. In particular, $S(q)$ at small q becomes constant for foams and equal to 1, indicating maximal randomness, for the Poisson patterns. Correspondingly, $h(D)$ at large D becomes $D/2$ for

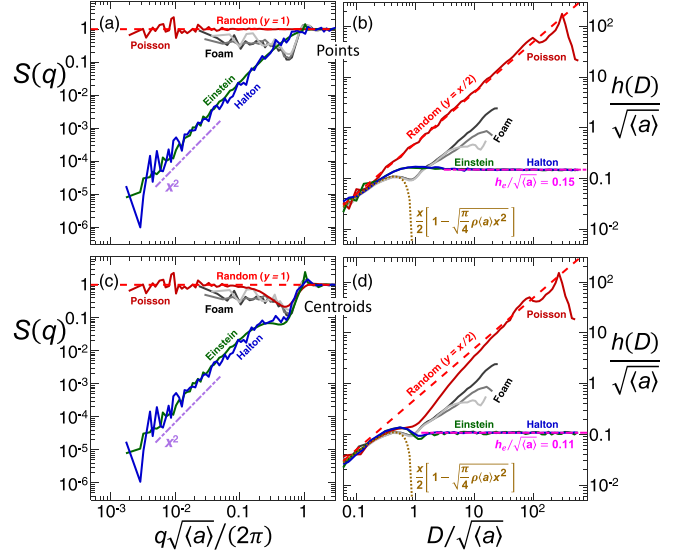


FIG. 7. Structure factor and associated real space hyperuniformity disorder length spectra for various point and centroid patterns as labeled. The foam data, for systems with $\langle a \rangle = \{10, 15, 25\}$ mm² as the curves go from dark to light gray, are the same in either (a) or (c) or (b) or (d) and have long-range Poissonian fluctuations. The data for the simulated point patterns are as follows: the Poisson data lie along the random expectation (red dashed line); the Halton or Einstein data are hyperuniform indicated by $h(D) = h_e$ (magenta dot-dashed line) and by the power-law decay of $S(0^+) \sim q^2$ (purple dot-dashed line). The centroid data are the same as the points data at long distances but there is an induced short-range order at short distances; this additional order is continued to long distances for the Einstein or Halton centroids indicated by a smaller value of h_e .

the Poisson patterns, and appears to be a smaller fraction of D for foams. The long-range nature of density fluctuations of bubble centroids is thus Poissonian but not totally random. The behavior is very different for the Einstein and Halton patterns: For small q and large D , their spectra scale as $S(q) \sim q^2$ and $h(D) = h_e$ (constant), and hence are hyperuniform; apparently, low discrepancy and hyperuniform are synonyms. The exponent $\epsilon = 2$ reproduces prior work on Einstein patterns [32], where the value of h_e was found to grow in proportion to the size of the RMS kick of the points from their lattice sites. Here, in fact, we selected this parameter in order to match the value of $h_e = 0.15\sqrt{\langle a \rangle}$ found for the Halton point patterns. This finding is helpful for intuitively understanding and evaluating the statistical uncertainty in a Monte Carlo integration using the Halton sequence: the variance is simply the average number of points that lie within h_e of the perimeter. While the long-range behavior of $h(D)$ for the Einstein and Halton patterns coincide, by construction, their structure factors could have been different and could have had different $\epsilon > 1$ exponents; it was thus a surprise that their $S(q)$ at small q match so well. Another finding, in Fig. 7(d), is that slightly smaller but in-common values of $h_e = 0.11\sqrt{\langle a \rangle}$ are found for the centroids of the Halton and Einstein Voronoi cells.

As for the short length scale behavior, all spectra in Fig. 7 asymptote to $S(q) = 1$ for large q and $h(D) = D/2$ for small D . With increasing D , the real space spectra for foam, Halton, and Einstein patterns all fall below this limit but lie above the

separated-particle limit set by $\sigma_\phi^2(D)/\phi = \langle a \rangle / [\pi(D/2)^2] - \phi$ for windows small enough to always contain only 0 or 1 point, at random, with probability set by window size and point density [28,32,33]. The foams spectra are found to be the smallest and closest to the separated-particle limit at the cellular scale, therefore they are the most uniform and least Poissonian. At larger scales, the foam spectra then turn up toward Poissonian behavior while the Halton and Einstein spectra develop hyperuniform signatures. It was a surprise that their spectra match so well at intermediate lengths.

2. Hyperuniformity of area fraction

An analysis that treats the patterns as cellular structures is similar but, we now compute the $\chi(q)$ and $h(D)$ spectra where the points and centroids are weighted by the areas of the cells they occupy. This quantifies fluctuations in area fraction measurements taken at different length scales. Since all the cellular patterns fill space, they are all hyperuniform by construction—even the Voronoi pattern constructed for the randomly placed points in the Poisson pattern. Thus the main question is to compare the ϵ exponents and the h_e values that respectively characterize the small- q and large- D asymptotics. This also tests the $\epsilon = 4$ prediction of Ref. [30].

Results for $\chi(q)$ and $h(D)$ for area-weighted points and centroids are collected in Fig. 8. At the smallest scales, for large q and small D , the spectra indicate random behavior as expected. Slightly away from this asymptotic behavior, the spectra all decrease but now without oscillations in the case of $\chi(q)$ and much more closely to the separated-particle limit in the case of $h(D)$. In fact, the $h(D)$ data in Fig. 8(d) for centroids collapse and follow this closely. By contrast the $h(D)$ data in Fig. 8(b) for points fan out with foam being smallest, and very closely matched to the separated-particle limit, while the Einstein and Halton data are nearly indistinguishable and lie between the foam and Poisson data. This corresponds to foam being most uniform and Poisson least uniform. The same ordering may be seen in the $\chi(q)$ data of Fig. 8(a), but less obviously. However, in Fig. 8(c), $\chi(q)$ is smallest at intermediate scales for the Halton pattern.

At the largest scales, for small q and large D , the area-weighted point and centroid pattern spectra all show tell-tale signs of hyperuniformity, as expected by construction. In particular, the $\chi(q)$ all vanish and the $h(D)$ all approach a constant, h_e . The values of h_e are different for the different patterns, and hence serve to quantify their relative degrees of uniformity. For foams, the value is given by $h_e/\sqrt{\langle a \rangle} = 0.084$. In Fig. 8(d), for the weighted centroids, essentially the same value is found for the Poisson patterns and slightly smaller values of $h_e/\sqrt{\langle a \rangle} = 0.080$ and $h_e/\sqrt{\langle a \rangle} = 0.076$ are found for the Einstein and Halton patterns. In Fig. 8(b), for the weighted points, the values are larger and indicated less uniformity: $h_e/\sqrt{\langle a \rangle} = 0.10$ for Einstein and Halton, and $h_e/\sqrt{\langle a \rangle} = 0.15$ for Poisson.

The asymptotic small- q behavior for the $\chi(q)$ spectra in Figs. 8(a), 8(c) is not as clear as for the $h(D)$ spectra. All are slightly concave up, except for the weighted points of the Poisson pattern in Fig. 8(a). It can hence be well fit with a pure power law, q^ϵ , which gives the exponent as $\epsilon = 3.5 \pm 0.1$. The foam data is least concave, and fits give $\epsilon = 4.2 \pm 0.2$.

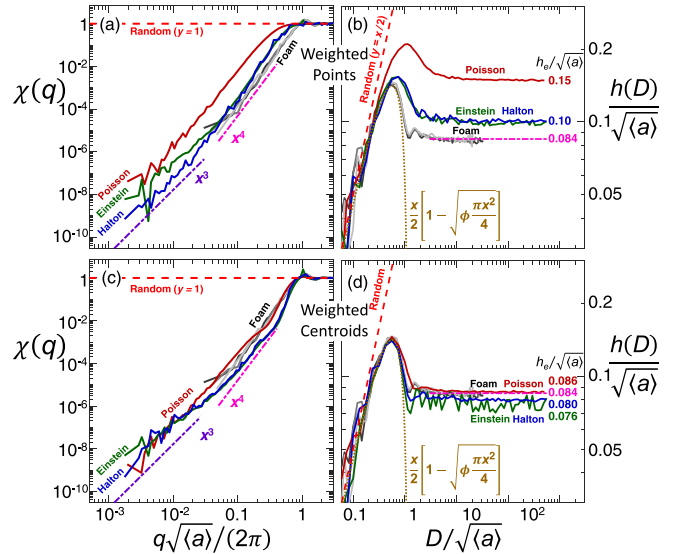


FIG. 8. Spectral density and associated hyperuniformity disorder length spectra for various cellular patterns as labeled. The foam data are for systems with $\langle a \rangle = \{10, 15, 25\}$ mm² as the curves go from dark to light gray and are the same in either (a) or (c) or (b) or (d). In (b), (d) the spectra of $h(D)$ for all patterns at intermediate and long lengths become constant and the values of h_e are labeled. These values are different depending on the disorder and h_e for the foam centroids is marked in both (b), (d) as a magenta dot-dashed line. The spectral density decays like $q^{4.2}$ for the foam data for all $q\sqrt{\langle a \rangle}/(2\pi) < 1$; for the Voronoi point and centroid data the $\chi(q)$ decay more slowly than the foam data but still have signatures of hyperuniformity. Only the foam data have a decay exponent near the $\epsilon = 4$ expectation determined in Ref. [30]. In (d), the $h(D)$ nearly collapse following the separated-particle limit (gold dotted curve) at small D and have very similar values of h_e .

The other spectra appear to cross over from $\epsilon \approx 4$ at intermediate q to $\epsilon \approx 3$ at smallest q . Recall that $\epsilon = 4$ was expected in all cases [30]. The discrepancies from prediction are noticeable, but not large, and are not understood.

3. Hyperuniformity of edges

We now turn attention to the lengths and locations of the cell edges, which are depicted in Figs. 2(e)–2(h). For foams, these are circular arcs literally made of thin aqueous soap films, which meet three at a time at 120° angles according to Plateau’s rules. This originates from surface tension, and the need to minimize cell perimeter at constant area. For the Voronoi constructions, the edges are fictitious straight line segments of zero thickness; they usually meet three at a time but at no prescribed angle.

The cumulative distribution of the length s of cell edges is shown in Fig. 9 as a function of s/\bar{s} where $\bar{s} = \sum s_i/N_s$ is the mean edge length and N_s is the total number of edges. As expected due to surface tension, foams have the narrowest distribution of edge lengths; this is juxtaposed with the fact that they have the broadest distribution of cell areas. The Poisson patterns have the widest distribution of edge lengths, which is also expected because of the large voids. The Halton and Einstein edge distributions are intermediate and very

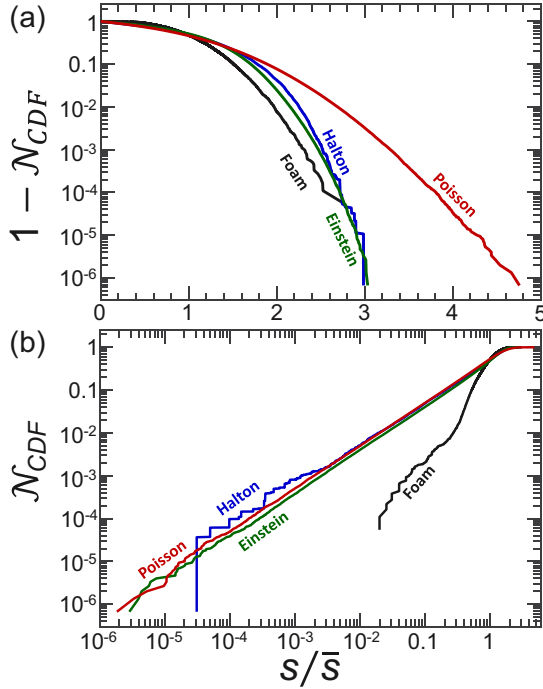


FIG. 9. The cumulative distribution function of edge lengths normalized by the mean edge length \bar{s} for types of system as labeled. The edges for the foams (Voronoi cells) are the films (walls) that connect two neighboring vertices on a bubble (Voronoi cell) and they are circular arcs (straight line segments). In (b) we show only the CDF on a log-log scale because the power-law scaling where $\mathcal{N}_{CDF} \sim s/\bar{s}$ for the very small Voronoi wall lengths is lost when the CDF is subtracted from 1.

similar to each other. The widths of the distributions may be quantified by the mean-squared edge length $\bar{s}^2 = \sum s_i^2/N_s$ divided by the mean edge length squared. Results are given in Table I, and are ordered as expected.

While Fig. 9(a) reveals the full distributions and their widths, it does not offer a good view of the preponderance of short edges. This is revealed better by the log-log plot of Fig. 9(b). There, $\mathcal{N}_{CDF} \sim s/\bar{s}$ is seen, with nearly the same proportionality constant, for all three types of the Voronoi construction. The foams behave quite differently, with far fewer short films. This may, perhaps, be explained in part by the quasi-2D nature of our samples, where edges that are shorter than the spacing between the plates can be eliminated by local rearrangements of the bubble packing.

As for the spatial distribution of edges, density fluctuations at different length scales may be quantified using the similar metrics as above. In particular, each edge is replaced by a point, located at the midpoint of the edge, and weighted by the length of the edge. Then the $\chi(q)$ and $h(D)$ spectra are computed and the results are displayed in Fig. 10. Lengths for each pattern are normalized $\langle s \rangle = \sum s_i^2 / \sum s_i$ where the sum is over all edges. As usual, the spectra show random behavior at the smallest length scales, while at intermediate scales $\chi(q)$ oscillates a bit and $h(D)$ hugs the separated-particle limit. The four pattern types are nearly indistinguishable across these lengths. At longer distances, the spectra for the Poisson pattern edges rises higher and faster than the others, indicating

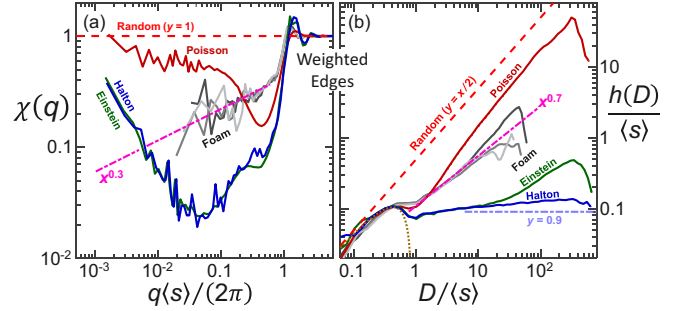


FIG. 10. Spectral density and associated hyperuniformity disorder length spectra for weighted edge patterns as labeled. In both parts the Poisson patterns show long-range random fluctuations but do not lie exactly on the random expectation (red dashed line). The Einstein and Halton patterns are not hyperuniform; this is more evident in the spectral density data where the data have clearly defined minima but (b) shows neither the Einstein nor the Halton data have $h(D) = h_e$ at large window sizes, which is evident by comparing the data to a fiduciary constant (dot-dashed line). The power law growth (magenta dot-dashed line) of $h(D) \sim D^{1-\epsilon}$ and $\chi(q) \sim q^\epsilon$ where $\epsilon = 0.3$ is consistent with a class of hyperuniform materials.

the greater fluctuations and lesser uniformity. The Halton and Einstein pattern spectra dip the lowest, indicating most uniformity, but then rise upwards—dramatically so for $\chi(q)$. The data even suggest that $\chi(q)$ rises to one for Poisson, Halton, and Einstein patterns, which would indicate completely random behavior at very large length scales greater than 1000 or more bubbles. This is actually reminiscent of spectra reported in Figs. 5(c), 5(e) of Ref. [28] for sphere packings very close to jamming. All this contrasts with the foam data, which at long lengths appear hyperuniform with power-law scaling of $\chi(q) \sim q^{0.3}$ and $h(D) \sim D^{0.7}$, where the exponent uncertainties are ± 0.15 . Since the foam systems cannot be made larger, we cannot rule out a turn up toward Poissonian behavior at extremely long length scales.

4. Hyperuniformity of foams

As a final exercise for the foam samples, Fig. 11 compares $\chi(q)$ and $h(D)$ fluctuation spectra for area-weighted centroids and length-weighted edge centers, shown earlier, as well for weighted vertices. To account for the spatial variation of the liquid phase, in analogy to the edge weighting, vertices are weighted by $\xi_i = \sum s_j/2$, the sum of half-lengths for the three connected edges; all lengths for the vertices are normalized by $\langle \xi \rangle = \sum \xi_i^2 / \sum \xi_i$. All spectra are averaged over the three ages, since the foams are in a self-similar scaling state. At small D (large q), all spectra appear random as expected. At intermediate (*i.e.* bubble) length scales, $h(D)$ hugs the separated-particle limit the most for centroids and the least for vertices. Over the same intermediate length scales, the three $\chi(q)$ spectra are similarly ranked, with vertices showing more disorder than films and films more disorder than centroids. At the longest length scales the weighted centroids are hyperuniform, since the foam cells are space filling, with $h(D) = 0.084\sqrt{\langle a \rangle}$ and $\chi(q) \sim q^{4.2 \pm 0.2}$. The films and vertices show evidence of weaker hyperuniformity, $\chi(q) \sim q^\epsilon$ and $h(D) \sim D^{1-\epsilon}$ with $\epsilon = 0.30 \pm 0.15$. However, it is hard to rule out

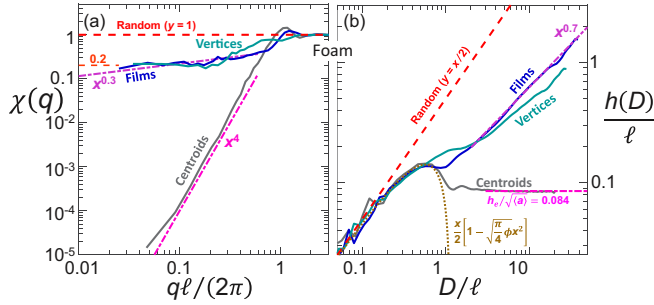


FIG. 11. Spectral density and associated hyperuniformity disorder length spectra for weighted patterns as labeled. All curves are the average of foam data at three different times. Lengths for the bubbles, films, and vertices are normalized by $\ell = \{\sqrt{\langle a \rangle}, \langle s \rangle, \langle \xi \rangle\}$, respectively. In both parts the bubbles exhibit strong hyperuniform behavior where the spectral density decays like $q^{4.2}$ and $h(D) = h_e$; the films have signatures of hyperuniform behavior where $h(D) \sim D^{1-\epsilon}$ and $\chi(q) \sim q^\epsilon$ where $\epsilon = 0.3$. For the vertices (a) shows the data level off to a constant $\chi(q) = 0.2$ indicating long range random fluctuations and (b) shows no clear signal.

$\chi(q) = 0.2$ Poissonian behavior for the films and vertices. Nevertheless, their $h(D)$ spectra are clearly sub-Poissonian for length scales ranging from 0.2 up to 30 or 40 bubble diameters.

IV. CONCLUSION

To what extent are foams hyperuniform, and do Plateau's laws confer additional uniformity? To explore such issues, we quantified the short- and long-range structure of a coarsening foam using $\chi(q)$ and $h(D)$, Hyperuniformity disorder length spectroscopy (HUDLS). And we compared against spectra for three other space-filling patterns. Of these, we find that the foams are the most locally disordered because they have the widest distribution of cell areas. However, this local structure does not inform the long-range uniformity. Using a recently defined emergent length scale, the hyperuniformity disorder length, we show the bubble centroids weighted by their areas as well as the Poisson, Halton, and Einstein points weighted by the areas of their Voronoi cells are all hyperuniform. This analysis also finds the weighted bubbles centroids are the most ordered; this is evidenced by $h(D) = h_e$ for all patterns, but the value of h_e is smallest for foams. Relocating the Voronoi points to the centroids of the Voronoi cells shows a near collapse in the values of h_e to that of the bubbles centroids. In

Fourier space, the weighted foams are also the most ordered when compared to any of the weighted Voronoi patterns; this is determined from the power-law behavior where $\chi(0^+) \sim q^\epsilon$ and $\epsilon = 4.2$ for the foams. This value, used as a proxy for long-range order, is the largest among all the patterns and only the foams have a decay exponent near the expected value $\epsilon = 4$ predicted in Ref. [30]. Additionally the foam edges are the only ones that have signatures of hyperuniformity in both real and Fourier space.

While the foam samples appear more ordered than the simulated cellular patterns, the latter have about 100×100 more cells than the number of bubbles we were able to study in the laboratory. It would be interesting to increase the foam system size and see if the apparent hyperuniformity persists, or if Poissonian features arise at extremely long distance, e.g., by an upturn of $\chi(q)$ at very small q or by an upturn of $h(D)$ at very large D . This would be difficult for both experiment and simulation. Another open question regards wet foams, where the bubbles do not entirely fill space. The decoration theorem holds that, in two dimensions, wet foam structure is obtained by decorating the vertices of a perfectly dry foam without shifting their positions [42]. This theorem fails if there exist films that are shorter than the extent of the decorated vertices, which is likely for large enough foams even if very dry. Therefore, the effect of variable wetness on long-range structure is nontrivial.

Besides foams we could use the hyperuniformity disorder length to determine long-range structure in other naturally occurring cellular patterns. This analysis can be used in two dimensions on networks made from cracks in dried mud, from peaks and valleys in crumpled paper, or from biological cells. In three dimensions one could study biological networks of trabecular bone or any other types of porous materials. A natural extension of our work is to perform analysis for three-dimensional foams. Experiments on 3D foams has found that they, like 2D foams, enter a self-similar scaling state [43]. Applying HUDLS to any of these systems offers a general and intuitive real space method to characterize the spectrum of structural features, which is a fundamental step in understanding material properties.

ACKNOWLEDGMENTS

We thank Nigel Goldenfeld for introducing us to low discrepancy sequences. This work was supported by NASA Grants No. 80NSSC19K0599 and No. 80NSSC21K0898 and by NSF Grant No. MRSEC/DMR-1720530.

- [1] D. Weaire and S. Hutzler, *The Physics of Foams* (Oxford University Press, New York, 2001).
- [2] J. A. Glazier and D. Weaire, The kinetics of cellular patterns, *J. Phys.: Condens. Matter* **4**, 1867 (1992).
- [3] J. Stavans, The evolution of cellular structures, *Rep. Prog. Phys.* **56**, 733 (1993).
- [4] H. Flyvbjerg, Model for coarsening froths and foams, *Phys. Rev. E* **47**, 4037 (1993).
- [5] J. Stavans, Temporal evolution of two-dimensional drained soap froths, *Phys. Rev. A* **42**, 5049 (1990).
- [6] J. Stavans, Evolution of two-dimensional cellular structures: The soap froth, *Physica A* **194**, 307 (1993).
- [7] J. Stavans and J. A. Glazier, Soap Froth Revisited: Dynamic Scaling in the Two-Dimensional Froth, *Phys. Rev. Lett.* **62**, 1318 (1989).
- [8] M. de Icaza, A. Jiménez-Ceniceros, and V. M. Castaño, Statistical distribution functions in 2d foams, *J. Appl. Phys.* **76**, 7317 (1994).
- [9] J. A. Glazier, M. P. Anderson, and G. S. Grest, Coarsening in the two-dimensional soap froth and the large- q

- potts model: A detailed comparison, *Philos. Mag. B* **62**, 615 (1990).
- [10] T. Herdtle and H. Aref, Numerical experiments on two-dimensional foam, *J. Fluid Mech.* **241**, 233 (1992).
- [11] D. Segel, D. Mukamel, O. Krichevsky, and J. Stavans, Selection mechanism and area distribution in two-dimensional cellular structures, *Phys. Rev. E* **47**, 812 (1993).
- [12] A. D. Rutenberg and M. B. McCurdy, Scaling state of dry two-dimensional froths: Universal angle-deviations and structure, *Phys. Rev. E* **73**, 011403 (2006).
- [13] L. Neubert and M. Schreckenberg, Numerical simulation of two-dimensional soap froth, *Physica A* **240**, 491 (1997).
- [14] S. Torquato and F. H. Stillinger, Local density fluctuations, hyperuniformity, and order metrics, *Phys. Rev. E* **68**, 041113 (2003).
- [15] C. E. Zachary and S. Torquato, Hyperuniformity in point patterns and two-phase random heterogeneous media, *J. Stat. Mech.: Theory Exp.* (2009) P12015.
- [16] S. Torquato, Hyperuniform states of matter, *Phys. Rep.* **745**, 1 (2018).
- [17] C. E. Zachary, Y. Jiao, and S. Torquato, Hyperuniform Long-Range Correlations are a Signature of Disordered Jammed Hard-Particle Packings, *Phys. Rev. Lett.* **106**, 178001 (2011).
- [18] C. E. Zachary, Y. Jiao, and S. Torquato, Hyperuniformity, quasi-long-range correlations, and void-space constraints in maximally random jammed particle packings. I. Polydisperse spheres, *Phys. Rev. E* **83**, 051308 (2011).
- [19] C. E. Zachary, Y. Jiao, and S. Torquato, Hyperuniformity, quasi-long-range correlations, and void-space constraints in maximally random jammed particle packings. II. Anisotropy in particle shape, *Phys. Rev. E* **83**, 051309 (2011).
- [20] R. Kurita and E. R. Weeks, Incompressibility of polydisperse random-close-packed colloidal particles, *Phys. Rev. E* **84**, 030401(R) (2011).
- [21] L. Berthier, P. Chaudhuri, C. Coulais, O. Dauchot, and P. Sollich, Suppressed Compressibility at Large Scale in Jammed Packings of Size-Disperse Spheres, *Phys. Rev. Lett.* **106**, 120601 (2011).
- [22] Y. Jiao, T. Lau, H. Hatzikirou, M. Meyer-Hermann, J. C. Corbo, and S. Torquato, Avian photoreceptor patterns represent a disordered hyperuniform solution to a multiscale packing problem, *Phys. Rev. E* **89**, 022721 (2014).
- [23] R. Dreyfus, Y. Xu, T. Still, L. A. Hough, A. G. Yodh, and S. Torquato, Diagnosing hyperuniformity in two-dimensional, disordered, jammed packings of soft spheres, *Phys. Rev. E* **91**, 012302 (2015).
- [24] J. H. Weijjs, R. Jeanneret, R. Dreyfus, and D. Bartolo, Emergent Hyperuniformity in Periodically Driven Emulsions, *Phys. Rev. Lett.* **115**, 108301 (2015).
- [25] S. Atkinson, G. Zhang, A. B. Hopkins, and S. Torquato, Critical slowing down and hyperuniformity on approach to jamming, *Phys. Rev. E* **94**, 012902 (2016).
- [26] Y. Wu, P. Olsson, and S. Teitel, Search for hyperuniformity in mechanically stable packings of frictionless disks above jamming, *Phys. Rev. E* **92**, 052206 (2015).
- [27] A. Ikeda and L. Berthier, Thermal fluctuations, mechanical response, and hyperuniformity in jammed solids, *Phys. Rev. E* **92**, 012309 (2015).
- [28] A. T. Chieco, M. Zu, A. J. Liu, N. Xu, and D. J. Durian, The spectrum of structure for jammed and unjammed soft disks, *Phys. Rev. E* **98**, 042606 (2018).
- [29] M. A. Klatt, J. Lovrić, D. Chen, S. C. Kapfer, F. M. Schaller, P. W. A. Schönhöfer, B. S. Gardiner, A. Smith, G. E. Schröder-Turk, and S. Torquato, Universal hidden order in amorphous cellular geometries, *Nature Commun.* **10**, 811 (2019).
- [30] J. Kim and S. Torquato, Methodology to construct large realizations of perfectly hyperuniform disordered packings, *Phys. Rev. E* **99**, 052141 (2019).
- [31] S. Torquato and D. Chen, Multifunctional hyperuniform cellular networks: Optimality, anisotropy and disorder, *Multifunct. Mater.* **1**, 015001 (2018).
- [32] A. T. Chieco, R. Dreyfus, and D. J. Durian, Characterizing pixel and point patterns with a hyperuniformity disorder length, *Phys. Rev. E* **96**, 032909 (2017).
- [33] D. J. Durian, Hyperuniformity disorder length spectroscopy for extended particles, *Phys. Rev. E* **96**, 032910 (2017).
- [34] D. Hexner, A. J. Liu, and S. R. Nagel, Two Diverging Length Scales in the Structure of Jammed Packings, *Phys. Rev. Lett.* **121**, 115501 (2018).
- [35] A. E. Roth, C. D. Jones, and D. J. Durian, Bubble statistics and coarsening dynamics for quasi-two-dimensional foams with increasing liquid content, *Phys. Rev. E* **87**, 042304 (2013).
- [36] A. T. Chieco and D. J. Durian, Experimentally testing a generalized coarsening model for individual bubbles in quasi-two-dimensional wet foams, *Phys. Rev. E* **103**, 012610 (2021).
- [37] J. H. Halton, Algorithm 247: Radical-inverse quasi-random point sequence, *Commun. ACM* **7**, 701 (1964).
- [38] J. H. Halton, On the efficiency of certain quasi-random sequences of points in evaluating multi-dimensional integrals, *Numer. Math.* **2**, 84 (1960).
- [39] H. Niederreiter, *Random Number Generation and quasi-Monte Carlo Methods* (Society for Industrial and Applied Mathematics, Philadelphia, 1992).
- [40] L. Kocis and W. J. Whiten, Computational investigations of low-discrepancy sequences, *ACM Trans. Math. Softw.* **23**, 266 (1997).
- [41] A. Okabe, B. Boots, K. Sugihara, and S. N. Chiu, *Spatial Tessellations: Concepts and Applications of Voronoi Diagrams*, Vol. 501 (John Wiley & Sons, New York, 2009).
- [42] F. Bolton and D. Weaire, The effects of plateau borders in the two-dimensional soap froth I. Decoration lemma and diffusion theorem, *Philos. Mag. B* **63**, 795 (1991).
- [43] J. Lambert, R. Mokso, I. Cantat, P. Cloetens, J. A. Glazier, F. Graner, and R. Delannay, Coarsening Foams Robustly Reach a Self-Similar Growth Regime, *Phys. Rev. Lett.* **104**, 248304 (2010).